

---

# UNPAIRED CROSS-DOMAIN CALIBRATION OF DMSP TO VIIRS NIGHTTIME LIGHT DATA BASED ON CUT NETWORK

---

**Zhan Tong**

College of Electrical Engineering  
Nanjing Institute of Technology  
Nanjing, Jiangsu 210000  
tz1390697164@outlook.com

**ChenXu Zhou**

College of Communication Engineering  
Nanjing Institute of Technology  
Nanjing, Jiangsu 210000  
effictrl@gmail.com

**Fei Tang**

College of Electrical Engineering  
Nanjing Institute of Technology  
Nanjing, Jiangsu 210000  
1542834053@qq.com

**Yiming Tu**

College of Electrical Engineering  
Nanjing Institute of Technology  
Nanjing, Jiangsu 210000  
1052720195@qq.com

**Tianyu Qin**

College of Electrical Engineering  
Nanjing Institute of Technology  
Nanjing, Jiangsu 210000  
1447335712@qq.com

**Kaihao Fang**

College of Resource and Environmental  
Anhui University  
Hefei, Anhui 230601  
1160405819@qq.com

March 18, 2026

## ABSTRACT

Defense Meteorological Satellite Program (DMSP-OLS) and Suomi National Polar-orbiting Partnership (SNPP-VIIRS) nighttime light (NTL) data are vital for monitoring urbanization, yet sensor incompatibilities hinder long-term analysis. This study proposes a cross-sensor calibration method using Contrastive Unpaired Translation (CUT) network to transform DMSP data into VIIRS-like format, correcting DMSP defects. The method employs multilayer patch-wise contrastive learning to maximize mutual information between corresponding patches, preserving content consistency while learning cross-domain similarity. Utilizing 2012–2013 overlapping data for training, the network processes 1992–2013 DMSP imagery to generate enhanced VIIRS-style raster data. Validation results demonstrate that generated VIIRS-like data exhibits high consistency with actual VIIRS observations ( $R^2 > 0.95$ ) and socioeconomic indicators. This approach effectively resolves cross-sensor data fusion issues and calibrates DMSP's defects, providing a reliable attempt for extended NTL time-series.

## 1 Introduction

The idea that city lights could serve as a proxy for human activity dates back to the mid-1990s, when Elvidge and colleagues first demonstrated a robust relationship between satellite-observed nighttime radiance and economic indicators such as GDP and electric power consumption [1]. Since then, nighttime light (NTL) remote sensing has evolved into a standard tool across disciplines—urbanization researchers use it to map informal settlements, economists employ it to estimate subnational productivity, and energy analysts draw upon it to model carbon emissions [2–5]. Yet this versatility hinges on data continuity, which remains elusive. The field currently relies on two incompatible sensors: the Defense Meteorological Satellite Program's Operational Linescan System (DMSP-OLS), operational from 1992 to 2013, and the Suomi NPP satellite's Visible Infrared Imaging Radiometer Suite (VIIRS), available from 2012 onward. The former offers temporal depth; the latter provides radiometric fidelity [6]. Bridging this gap is not merely a technical convenience but a prerequisite for any longitudinal analysis of anthropogenic change.

The obstacles to direct integration are substantial and, in some respects, fundamental [7]. DMSP-OLS was never designed for quantitative radiometry: its spatial resolution (1 km) blurs fine-scale settlement patterns, its lack of on-board calibration renders cross-sensor comparison hazardous, and its 6-bit quantization imposes a hard saturation ceiling at  $DN=63$  that obliterates contrast in dense urban cores [8]. VIIRS corrects these deficiencies—finer resolution (500 m), radiometric calibration, 14-bit dynamic range—but at the weakness of temporal coverage [9]. Additional complications

arise from orbital drift and spectral band differences that introduce subtle but systematic discontinuities [10]. Simple concatenation of the two records thus produces spurious trends that confound interpretation.

Conventional calibration strategies have approached this problem through statistical regression against pseudo-invariant features (PIF), typically employing linear, power-law, or sigmoid transfer functions to map between DMSP digital numbers and VIIRS radiance units [11–13]. These methods preserve broad temporal patterns but fail to address the saturation problem in any meaningful way; bright urban centers remain clipped and featureless [14]. More fundamentally, pixel-wise regression ignores spatial context—it treats each location as an independent observation, neglecting the topological relationships that define urban structure [15]. Recent efforts to incorporate auxiliary information, such as Enhanced Vegetation Index (EVI) to modulate saturation correction [16], represent incremental improvements, yet the conversion process continues to sacrifice spatial detail.

Deep learning offers a conceptual departure. Image-to-image translation networks, originally developed for photographic style transfer, have recently been adapted for cross-sensor calibration [17]. Autoencoder architectures and U-Net variants can learn nonlinear mappings that statistical methods cannot capture [9, 15]. Chen et al., for example, trained an AE model with EVI constraints to generate synthetic VIIRS data from DMSP inputs, extending the high-quality record forward to 2000 [9]. Others have pursued the inverse problem, downgrading VIIRS to DMSP-like characteristics for forward extension [7, 15]. These approaches achieve lower residual errors than regression-based methods, but they share a common limitation: reliance on cycle-consistency or paired training data that assumes an invertible, one-to-one correspondence between sensor domains [18]. This assumption becomes problematic when translating from DMSP to VIIRS, where the task is essentially hallucinating high-frequency detail that does not exist in the source. Enforcing bidirectional consistency in such cases risks distorting content or suppressing legitimate spatial variation.

We adopt a different strategy. This paper proposes a cross-sensor calibration framework based on Contrastive Unpaired Translation (CUT) [18], which abandons the cycle-consistency requirement entirely. CUT employs a patch-wise contrastive loss (PatchNCE) to maximize mutual information between corresponding local regions of input and output images, enabling one-directional translation without inverse reconstruction [18]. For DMSP-to-VIIRS conversion, this architecture is particularly well-suited: it preserves the spatial structure present in the original DMSP imagery while learning to synthesize VIIRS-appropriate radiometric textures, rather than forcing a bijective mapping that the sensor physics do not support.

To address these limitations, this study proposes a methodological transition from cycle-consistent frameworks to contrastive unpaired translation. While CycleGAN [19] and its derivatives have demonstrated efficacy in general domain adaptation, their foundational assumption of bijective mapping—enforced via cycle-consistency loss—exhibits limited applicability to cross-sensor radiometric calibration. Similarly, paired approaches such as Pix2Pix [20] necessitate strictly spatially-registered image pairs, which are unattainable for heterogeneous sensors characterized by divergent spatial resolutions and temporal coverage. The translation from DMSP to VIIRS constitutes an inherently asymmetric mapping: the task requires synthesizing high-frequency spatial details and radiometric gradients that are physically absent in the source domain, rather than merely restyling existing content. Imposing a reverse mapping constraint (VIIRS  $\rightarrow$  DMSP) under such conditions risks suppressing legitimate structural variations or introducing systematic artifacts, as the model struggles to compress enhanced VIIRS-resembling features into the saturated, low-bit DMSP representation. By eliminating the cycle-consistency constraint, CUT [18] facilitates unidirectional mapping, enabling the model to concentrate on optimizing the fidelity of the forward mapping while circumventing optimization conflicts inherent to bidirectional training. Furthermore, the core mechanism of CUT—Patch-wise Noise Contrastive Estimation (PatchNCE)—provides a theoretically-grounded solution for maintaining spatial fidelity during radiometric enhancement. In contrast to the pixel-wise L1/L2 losses employed by Pix2Pix [20], which tend to yield blurred outputs, and the global adversarial losses utilized by CycleGAN [19], which may compromise local structural consistency, PatchNCE maximizes mutual information between corresponding local patches across input and output domains while repelling non-corresponding patches. This contrastive objective ensures that the translated imagery retains the topological structure and spatial context of the original DMSP observations (e.g., urban boundaries, road networks) while adapting its radiometric distribution to conform to VIIRS characteristics. Critically, this patch-level contrast operates across multiple encoder layers, permitting the model to align low-level textures and high-level semantic features in a coordinated manner without requiring paired training data. For long-term NTL time series construction, where geometric consistency across decades is paramount, this content-preserving property renders CUT methodologically advantageous relative to regression-based or cycle-consistent alternatives.

## 2 Study Area and Data

### 2.1 Study Object

The primary objective of this study is to construct a seamless, long-term Nighttime Light (NTL) time series spanning from 1992 to 2020. The study focuses on anthropogenic lighting sources associated with human settlements, including urban cores, suburban areas, and major transportation networks. Given the global coverage of the Defense Meteorological Satellite Program (DMSP) and Suomi National Polar-orbiting Partnership (Suomi NPP) satellites, our framework is designed to be globally applicable. However, to ensure the robustness of the cross-sensor calibration, we prioritize regions with stable human activity and minimal seasonal vegetation interference. The temporal scope covers the entire operational lifespan of DMSP-OLS (1992–2013) and extends through the VIIRS era (2012–2020), with a specific focus on the overlap year of 2013 for model training and validation.

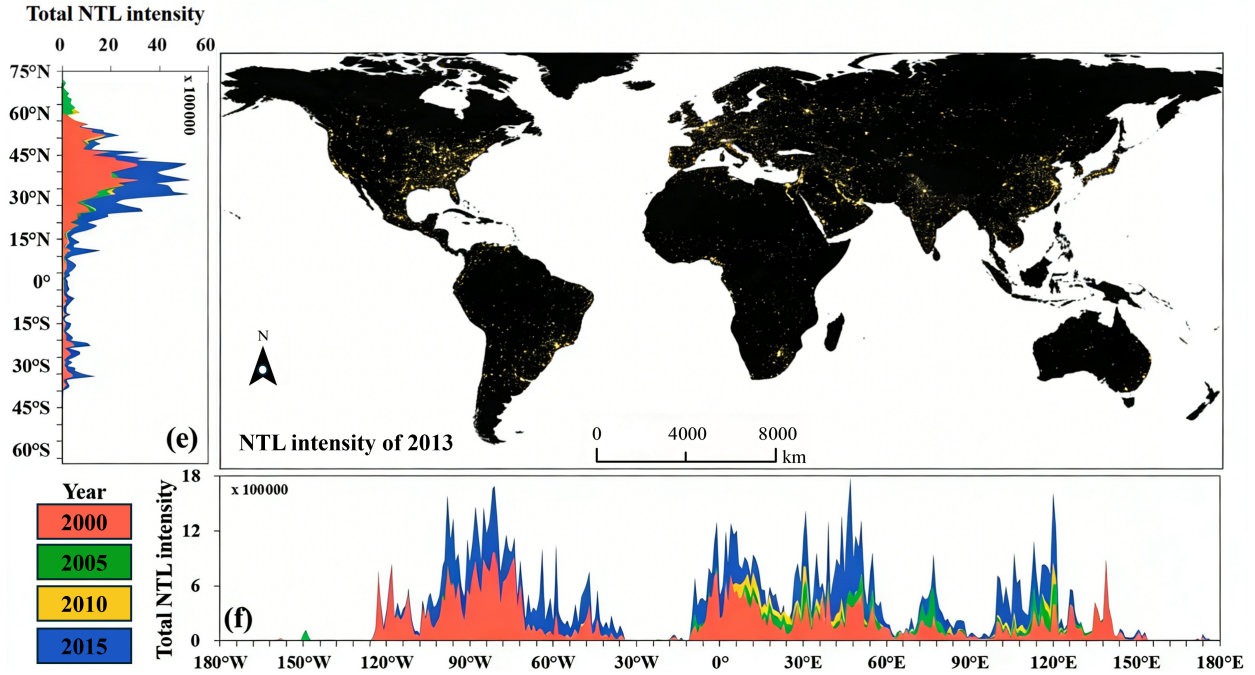


Figure 1: NTL visualization and cumulative analysis of longitude and latitude

### 2.2 Data Sources

This study utilizes two distinct generations of satellite-derived nighttime light data: the DMSP-OLS Operational Linescan System and the VIIRS Day/Night Band (DNB). These sensors represent the standard for long-term NTL analysis but differ significantly in their radiometric and spatial characteristics. Table 1 summarizes the key technical specifications of both sensors.

#### 2.2.1 DMSP-OLS Data

The DMSP-OLS data were acquired from the National Geophysical Data Center (NGDC) Version 4 Archive. This dataset includes annual composite images generated from multiple satellites (F10–F18) spanning 1992 to 2013. The standard product undergoes cloud masking and removal of ephemeral lights (e.g., fires), but lacks on-board radiometric calibration. The digital numbers (DN) range from 0 to 63, with significant saturation observed in dense urban centers. For the calibration overlap period, we utilize data from the F18 satellite (2013), which offers the most recent sensor characteristics prior to the system’s retirement. The data are resampled to a 30 arc-second grid (approximately 1 km at the equator) for consistency with existing literature [1].

Table 1: Technical comparison between DMSP-OLS and Suomi NPP VIIRS sensors.

Parameter	DMSP-OLS	Suomi NPP VIIRS
<b>Operator</b>	U.S. Air Force	NASA-NOAA (JPSS)
<b>Update period</b>	Annual	monthly
<b>Orbit</b>	Polar Sun-Synchronous (850 km, 98.8°)	Polar Sun-Synchronous (827 km, 98.7°)
<b>Revisit Time</b>	102 minutes	102 minutes
<b>Swath Width</b>	3,000 km	3,000 km
<b>Local Overpass Time</b>	~19:30 (Descending, pre-2013)	~01:30 (Descending)
<b>Spectral Range</b>	0.5–0.7 $\mu\text{m}$ (Panchromatic)	0.5–0.9 $\mu\text{m}$ (DNB)
<b>Native Resolution</b>	5 km $\times$ 5 km (Nadir)	742 m $\times$ 742 m (Nadir)
<b>Product Resolution</b>	30 arc-seconds (~1 km)	500 m (VCMCFG)
<b>Quantization</b>	6-bit (0–63 DN)	14-bit
<b>Saturation</b>	Common in urban cores (DN=63)	No saturation
<b>Detection Limit</b>	$\sim 5 \times 10^{-10}$ W/cm <sup>2</sup> /sr	$\sim 2 \times 10^{-11}$ W/cm <sup>2</sup> /sr
<b>Radiometric Calibration</b>	None (Relative)	On-board (Solar Diffuser)
<b>Status</b>	Retired	Operational (JPSS-1/2+)

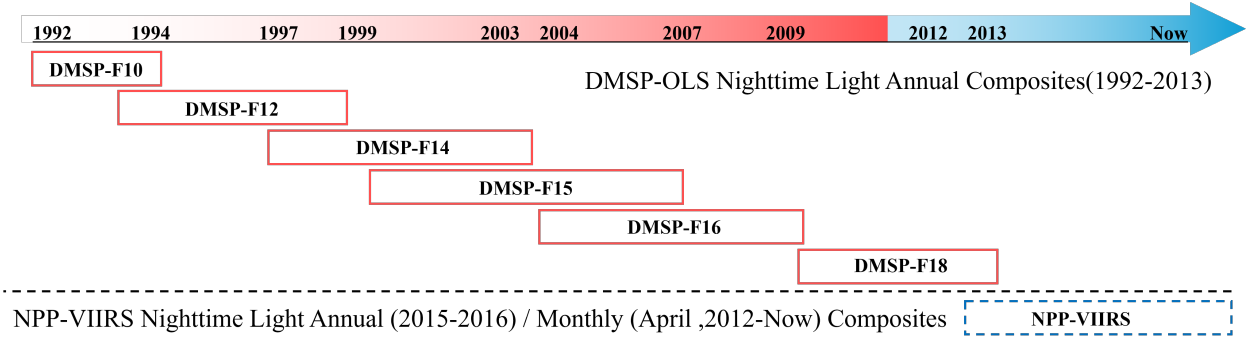


Figure 2: NTL data from DMSP-OLS and NPP-VIIRS

### 2.2.2 VIIRS DNB Data

The VIIRS Day/Night Band data are obtained from the NOAA National Centers for Environmental Information (NCEI). Specifically, we use the VCMCFG (Cloud-Free Coverages) annual composite product, which provides radiance values in units of  $\text{nW}\cdot\text{cm}^{-2}\cdot\text{sr}^{-1}$ . Unlike DMSP, VIIRS features on-board calibration via a solar diffuser, a wider dynamic range (14-bit), and a finer spatial resolution. The later overpass time (~01:30 local time) compared to DMSP (~19:30) captures different human activity patterns, introducing systematic differences in lighting intensity that must be accounted for during calibration [21]. The data are processed at a 500 m spatial resolution, offering detailed structural information of urban fabrics.

### 2.2.3 Auxiliary Data

To facilitate sample filtering and spatial analysis, we incorporate a global land mask derived from the Moderate Resolution Imaging Spectroradiometer (MODIS) land cover product. This mask is used to exclude ocean bodies, permanent ice sheets (latitude  $> 60^\circ$ ), and other non-settlement areas during the patch extraction phase. Additionally, population density grids from the Gridded Population of the World (GPW) v4 are used for independent validation of the calibrated NTL product against socioeconomic indicators.

## 2.3 Data Preprocessing

The preprocessing pipeline was designed to address three core challenges: (1) spatial misalignment between DMSP-OLS and VIIRS, (2) the extreme imbalance between informative urban patches and featureless background, and (3) the radiometric distribution mismatch that complicates direct network training. Figure 3 outlines the overall workflow.

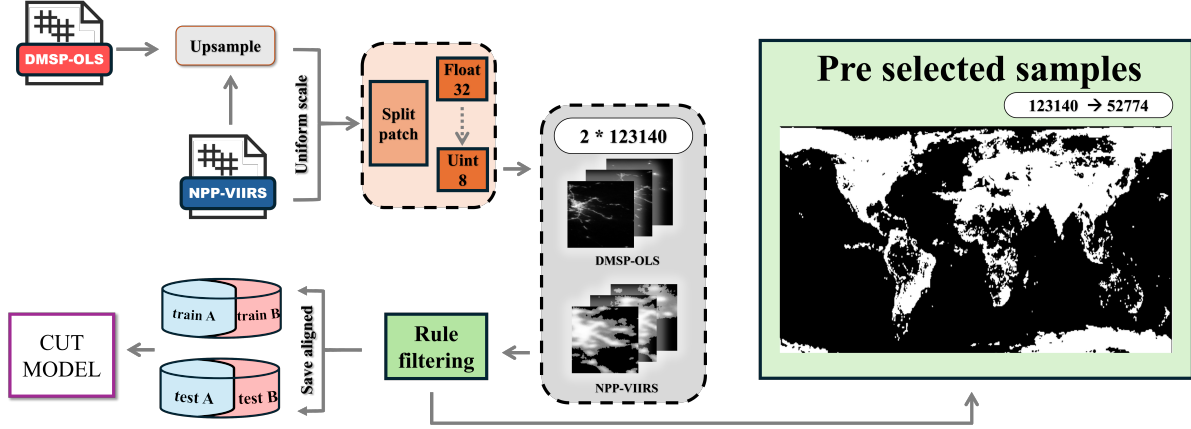


Figure 3: Schematic of the preprocessing workflow. The pipeline consists of resolution alignment, patch extraction with spatial filtering, radiometric distribution analysis, and format conversion for network training.

### 2.3.1 Resolution Alignment via Upsampling

DMSP-OLS and VIIRS differ in native spatial resolution (approximately 1 km vs. 500 m at the equator). To enable pixel-wise comparison and patch-based training, we upsampled the DMSP-OLS data to match the VIIRS grid. Using ArcGIS Pro’s `Resample_management` tool with bilinear interpolation, we transformed the original DMSP grid ( $0.00833^\circ$ ,  $43201 \times 16801$  pixels) to the VIIRS reference resolution ( $0.00416^\circ$ ,  $86402 \times 33602$  pixels). The upsampled product preserves the original radiometric values while providing geometric compatibility for subsequent patch extraction. Table 2 summarizes the resampling parameters and output statistics.

Table 2: Resampling parameters and output verification for DMSP-OLS upsampling.

Property	Original DMSP	Upsampled DMSP
Pixel size ( $^\circ$ )	0.0083333333	0.0041666667
Width (pixels)	43,201	86,402
Height (pixels)	16,801	33,602
Total pixels	725.8 M	2,903.2 M
Data type	Float32	Float32

### 2.3.2 Patch Extraction and Spatial Filtering

After resolution alignment, both datasets were partitioned into  $256 \times 256$  non-overlapping patches, yielding 52,774 paired samples per sensor. To focus computational resources on human settlements and reduce background noise, we applied a two-stage spatial filter:

1. **Land-ocean masking.** Using a MODIS-derived land mask, we excluded patches with land coverage  $< 30\%$ . This threshold was chosen empirically to retain coastal urban areas (e.g., Shanghai, New York) while discarding open ocean and sparsely populated regions.
2. **Polar region exclusion.** Patches centered at latitudes  $> 60^\circ$  were removed to avoid seasonal illumination artifacts and minimal anthropogenic lighting in high-latitude zones.

After spatial filtering, approximately 30% of the original patches were retained (15,832 samples), which formed the candidate pool for radiometric screening.

### 2.3.3 Radiometric Distribution Analysis and Outlier Filtering

A critical observation from exploratory analysis was the highly skewed radiometric distribution of both sensors, particularly the long tail of bright urban cores in VIIRS and the saturation ceiling in DMSP. Figure 4 shows the log-transformed histograms and cumulative distribution functions (CDFs) for both datasets.

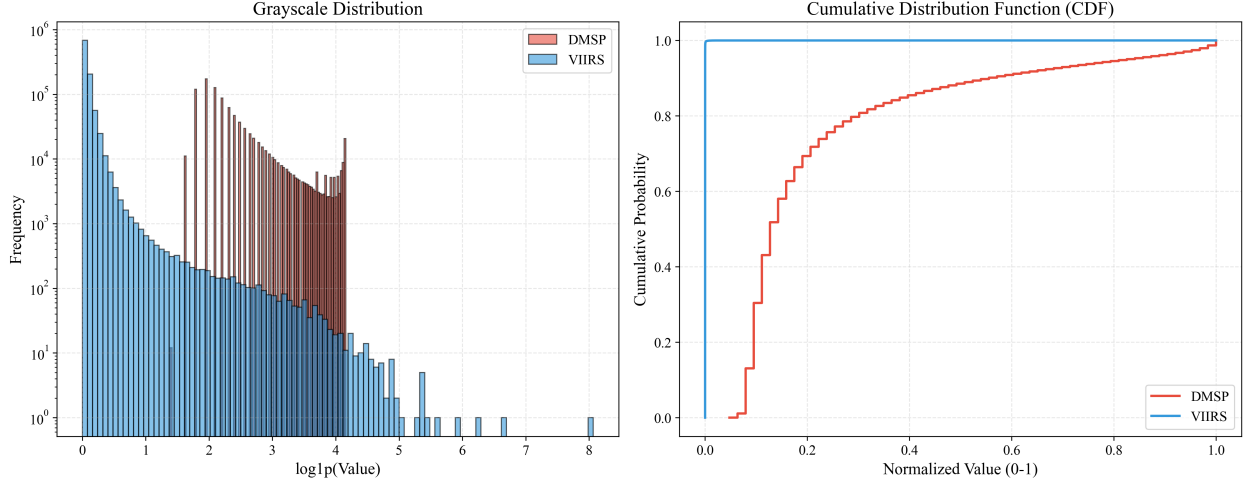


Figure 4: Radiometric distribution analysis. Top: histograms with  $\log_{1p}$  transformation to visualize long-tail behavior. Bottom: cumulative distribution functions. Vertical dashed lines indicate the 99.9th percentile thresholds used for outlier clipping.

Based on the CDF analysis, we adopted the 99.9th percentile as a robust clipping threshold to suppress extreme outliers (e.g., gas flares, transient lights) while preserving the dynamic range of urban lighting:

$$v_{\max}^{\text{DMSP}} = 4.1589 \quad (\log_{1p}(63)), \quad v_{\max}^{\text{VIIRS}} = 4.3643 \quad (\log_{1p}(77.6)). \quad (1)$$

Patches with mean radiance below  $\tau_{\text{dark}} = 0.1$  ( $\log_{1p}$  scale) or standard deviation below  $\tau_{\text{uniform}} = 0.05$  were further removed as featureless backgrounds. After radiometric filtering, the final training set comprised 12,417 high-quality paired patches.

### 2.3.4 Data Formatting for Network Training

Although the CUT framework theoretically supports floating-point inputs, our preliminary experiments indicated that training with raw Float32 radiance values led to unstable convergence and overfitting on high-intensity outliers. Following common practice in GAN-based image translation [19, 20], we normalized the clipped radiance values to the  $[0, 255]$  range and converted them to `uint8` format:

$$I_{\text{uint8}} = \left\lfloor 255 \times \frac{\log_{1p}(I) - v_{\min}}{v_{\max} - v_{\min}} \right\rfloor, \quad (2)$$

where  $v_{\min}$  and  $v_{\max}$  are the 0.1th and 99.9th percentiles of the  $\log$ -transformed radiance, respectively. This transformation compresses the dynamic range while preserving relative contrast, which stabilizes adversarial training. The corresponding inverse transformation is applied during inference to recover radiometrically meaningful outputs.

To accommodate single-channel NTL data in the original CUT codebase (designed for RGB images), we modified four core modules: (1) `data/unaligned_dataset.py` to skip RGB conversion and apply custom normalization, (2) `models/networks.py` to adjust input/output channels from 3 to 1, (3) `util/get_transform.py` to redefine the `ToTensor` operation for Float32 inputs, and (4) `data/image_folder.py` to recognize `.tif` extensions. These changes are documented in the public repository accompanying this work.

### 2.3.5 Training/Validation/Test Split with Spatial Independence

To prevent spatial autocorrelation from inflating performance metrics, we partitioned the dataset by geographic blocks rather than random sampling. The study area was divided into  $5^\circ \times 5^\circ$  tiles, which were randomly assigned to training (70%), validation (15%), and test (15%) sets. This ensures that patches in the test set are geographically disjoint from training samples, providing a more realistic assessment of generalization to unseen regions. Table 3 summarizes the final dataset composition.

Table 3: Final dataset composition after preprocessing and spatial partitioning.

Split	Number of Patches	Geographic Coverage	Purpose
Training	57,316	Global (stratified)	Model optimization
Validation	14,329	Global (stratified)	Hyperparameter tuning
Test	14,329	Held-out regions	Final evaluation
<b>Total</b>	<b>12,417</b>	<b>Global land areas</b>	

### 3 Methodology

#### 3.1 Problem Formulation

We formulate the DMSP-to-VIIRS radiometric calibration as an unpaired image-to-image translation problem. Let  $X_{\text{DMSP}}$  and  $Y_{\text{VIIRS}}$  denote the source and target domains, respectively. Our goal is to learn a mapping  $G : X_{\text{DMSP}} \rightarrow Y_{\text{VIIRS}}$  that transforms DMSP-OLS imagery into radiometrically consistent VIIRS-like outputs without requiring pixel-aligned training pairs.

The two domains exhibit substantial differences in spatial and radiometric characteristics (Table 4). DMSP-OLS data, even after upsampling to 500 m resolution, retain their original 6-bit quantization (DN values 0–63) with pervasive saturation in urban cores. In contrast, VIIRS DNB provides 14-bit radiance measurements (units:  $\text{nW}\cdot\text{cm}^{-2}\cdot\text{sr}^{-1}$ ) with a detection limit approximately 25 times lower than DMSP. To bridge this gap, we apply a log-transform  $\log_{1p}(x) = \log(1 + x)$  to compress the dynamic range, followed by normalization to  $[0, 255]$  for network training. The inverse transformation recovers physically meaningful radiance values during inference.

Table 4: Radiometric and spatial characteristics of DMSP-OLS and VIIRS DNB data after preprocessing.

Property	DMSP-OLS	VIIRS DNB
Resolution (after alignment)	500 m	500 m
Image dimensions	$86,402 \times 33,602$	$86,401 \times 33,601$
Raw value range	$[0.00, 63.00]$	$[-1.50, 85,588.98]$
$\log_{1p}$ 99.9th percentile	4.1589	4.3643
Quantization	6-bit (saturated)	14-bit (linear)

#### 3.2 Network Architecture

Our framework adopts the Contrastive Unpaired Translation (CUT) architecture [18], which replaces the cycle-consistency constraint with a patchwise contrastive loss to preserve spatial structure during domain translation. The overall design comprises three components: a generator for image translation, a discriminator for adversarial training, and a feature projection network for contrastive learning.

The generator follows a ResNet-based encoder-decoder design with 9 residual blocks. Since nighttime light data are single-channel rather than RGB, we reconfigured all convolutional layers to accept grayscale input, reducing the parameter count by approximately two-thirds. The network uses 64 base filters, doubling at each downsampling stage, with batch normalization and ReLU activation throughout. Reflection padding minimizes boundary artifacts that could interfere with patch-level feature extraction.

For adversarial training, we employ a PatchGAN classifier [20] that evaluates  $70 \times 70$  overlapping patches rather than classifying the entire image. This design choice focuses the discriminator on local texture consistency, which aligns well with our objective of preserving fine-scale urban structures. The discriminator consists of three convolutional layers with increasing filter counts ( $64 \rightarrow 128 \rightarrow 256$ ) and uses LeakyReLU activation (slope=0.2) to maintain gradient flow during training.

Figure 5 illustrates the complete network pipeline. The generator receives a DMSP patch and produces a VIIRS-like output, which is then evaluated by both the discriminator and the contrastive loss module. Unlike CycleGAN, which enforces bidirectional mapping through reconstruction, CUT performs unidirectional translation guided by feature-level correspondence. This asymmetry better matches the nature of cross-sensor calibration, where the target domain (VIIRS) contains information that simply does not exist in the source domain (DMSP).

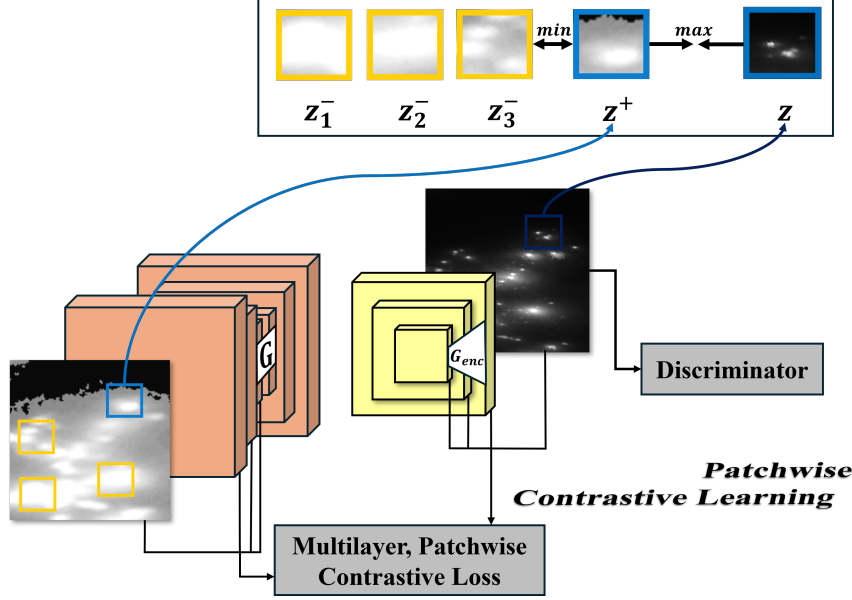


Figure 5: Overall network pipeline. The generator  $G$  translates DMSP to VIIRS-like imagery, while the discriminator distinguishes real from fake samples. Multilayer patchwise contrastive loss operates on intermediate features to ensure spatial consistency without requiring cycle reconstruction.

Several practical adaptations distinguish our implementation from the original CUT codebase. All data I/O operations handle single-channel GeoTIFF files with georeferencing metadata preserved for downstream analysis. The global-scale imagery ( $86,402 \times 33,602$  pixels) is too large for direct processing, so we extract non-overlapping  $256 \times 256$  patches during training. To prevent spatial autocorrelation from inflating performance metrics, training, validation, and test sets are stratified by geographic blocks rather than randomly sampled. This ensures that test patches come from regions the model has never encountered during training.

### 3.3 Loss Functions

The training objective combines adversarial and contrastive terms:

$$\mathcal{L}_{\text{total}} = \lambda_{\text{GAN}} \mathcal{L}_{\text{GAN}} + \lambda_{\text{NCE}} \mathcal{L}_{\text{NCE}}, \quad (3)$$

with  $\lambda_{\text{GAN}} = 1.0$  and  $\lambda_{\text{NCE}} = 1.0$  in our experiments. We also evaluated the FastCUT configuration ( $\lambda_{\text{NCE}} = 10.0$ ), which prioritizes content preservation at the cost of longer training time.

For the adversarial component, we adopt the Least Squares GAN (LSGAN) formulation [22]:

$$\mathcal{L}_{\text{GAN}}(G, D) = \mathbb{E}_{y \sim Y} \left[ \frac{1}{2} (D(y) - 1)^2 \right] + \mathbb{E}_{x \sim X} \left[ \frac{1}{2} D(G(x))^2 \right]. \quad (4)$$

Compared to standard GAN loss, LSGAN penalizes samples far from the decision boundary more heavily. This reduces gradient vanishing during late-stage training and produces sharper output—a desirable property for recovering saturated urban cores in DMSP data.

The PatchNCE loss forms the core of our approach. Rather than enforcing cycle-consistency through pixel-level reconstruction, it preserves spatial structure by maximizing mutual information between corresponding image patches. For each query patch extracted from the generated image  $\hat{y} = G(x)$ , the loss identifies a positive sample at the same spatial location in the input  $x$ , along with multiple negative samples from different locations. The contrastive objective then pulls the query toward its positive match while pushing it away from the negatives.

Figure 6 depicts the contrastive learning process. Features are extracted from five generator layers (indices 0, 4, 8, 12, 16), capturing information at multiple scales—from fine textures in early layers to coarse semantic structures in deeper layers. Each layer’s features pass through a two-layer MLP projection head:

$$f = \text{L2Norm}(\text{Linear}_2(\text{ReLU}(\text{Linear}_1(h))))), \quad (5)$$

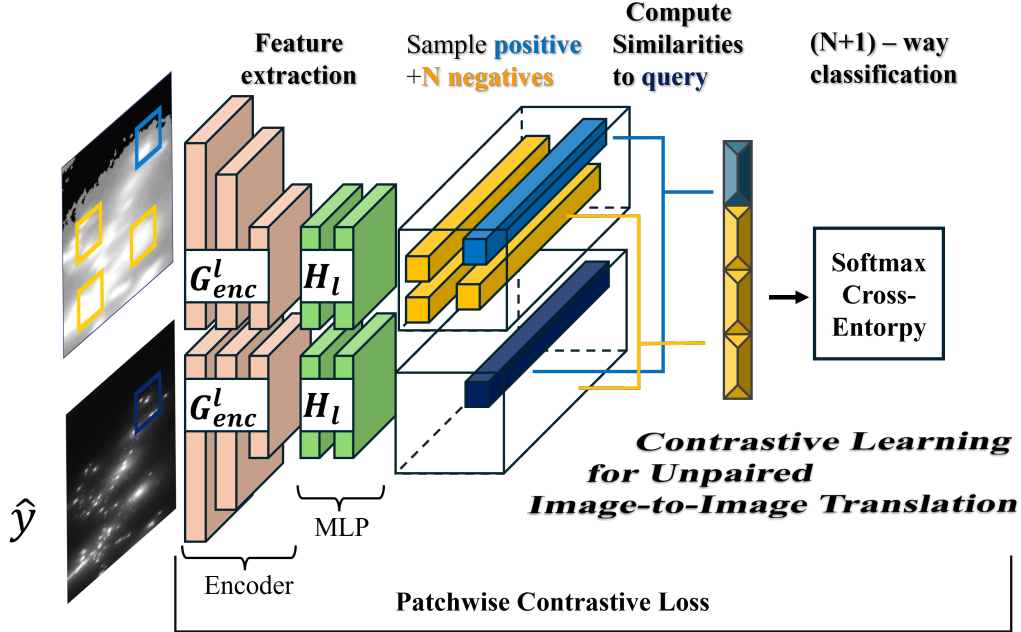


Figure 6: Patchwise contrastive learning mechanism. Features are extracted from both domains at multiple network depths, projected through MLP heads into a 256-dimensional embedding space, and compared via softmax cross-entropy. Positive pairs (blue) come from the same spatial location; negative pairs (yellow) come from different locations.

producing a 256-dimensional embedding  $f$  on the unit hypersphere. The contrastive loss is then computed as:

$$\mathcal{L}_{\text{NCE}} = \sum_{l=1}^L \sum_{p=1}^P -\log \frac{\exp(f_q^{(l,p)} \cdot f_{k_+}^{(l,p)} / \tau)}{\exp(f_q^{(l,p)} \cdot f_{k_+}^{(l,p)} / \tau) + \sum_{n=1}^N \exp(f_q^{(l,p)} \cdot f_{k_-}^{(l,n)} / \tau)}, \quad (6)$$

where  $\tau = 0.07$  is the temperature parameter and  $N = 255$  negative samples are used per query.

The geographic consistency preservation emerges naturally from this formulation. By anchoring positive pairs to identical coordinates  $(i, j)$  in both domains, the loss implicitly aligns urban boundaries, road networks, and settlement patterns without explicit geometric constraints. The multi-scale nature of the loss—applied across five generator layers—ensures that both local textures and global structures remain coherent after translation. Negative sampling prevents the generator from collapsing to mode averaging, which would otherwise blur distinct lighting patterns into homogeneous outputs. For cross-sensor calibration, this mechanism enables the network to hallucinate high-frequency details absent in DMSF while maintaining the original spatial layout—a capability that cycle-consistent methods struggle to achieve.

### 3.4 Implementation Details

All experiments were conducted on an NVIDIA GeForce RTX 5070 Ti GPU with CUDA 12.4, using PyTorch 2.5.1 (Python 3.11). We modified the official CUT codebase<sup>1</sup> to support single-channel GeoTIFF inputs and adjusted the data loading pipeline for large-scale remote sensing imagery.

Training uses the Adam optimizer with  $\beta_1 = 0.5$  and  $\beta_2 = 0.999$ . The learning rate is held at  $2 \times 10^{-4}$  for 200 epochs, then linearly decayed to zero over the next 200 epochs. We use a batch size of 4, which fits comfortably within the 16 GB VRAM of our GPU while providing sufficient gradient stability. Each epoch processes approximately 8,700 training patches and takes about 12 minutes to complete.

Data augmentation is kept minimal to preserve radiometric fidelity. Random horizontal flipping (probability 0.5) is applied during training, but we avoid color jitter (not applicable to single-channel data) and geometric deformations (which would distort spatial relationships). The random seed is fixed at 42 to ensure reproducibility across runs.

<sup>1</sup><https://github.com/taesungp/contrastive-unpaired-translation>

Table 5: Training hyperparameters for the CUT-based calibration model.

Parameter	Value
Optimizer	Adam ( $\beta_1 = 0.5, \beta_2 = 0.999$ )
Initial learning rate	$2 \times 10^{-4}$
LR schedule	Linear decay after epoch 200
Total epochs	400
Batch size	4
Patch size	$256 \times 256$
NCE layers	0, 4, 8, 12, 16
NCE patches per layer	256
Temperature $\tau$	0.07
Feature dimension	256
GAN mode	LSGAN
Weight initialization	Normal ( $\mu = 0, \sigma = 0.02$ )

Models are saved every 5 epochs, with the best validation checkpoint retained for final evaluation. Training progress is monitored through loss curves ( $\mathcal{L}_{GAN}$ ,  $\mathcal{L}_{NCE}$ , discriminator accuracy), GPU utilization metrics, and visual samples generated every 1,000 iterations. Total training time for 400 epochs is approximately 80 hours. The trained model and preprocessing scripts are available at our project repository.

## 4 Experiments and Results

### 4.1 Training Convergence Analysis

Figure 7 shows the training loss curves over 2,800 iterations. Both the NCE loss and GAN loss exhibit stable convergence patterns after an initial sharp decline in the first 500 iterations.

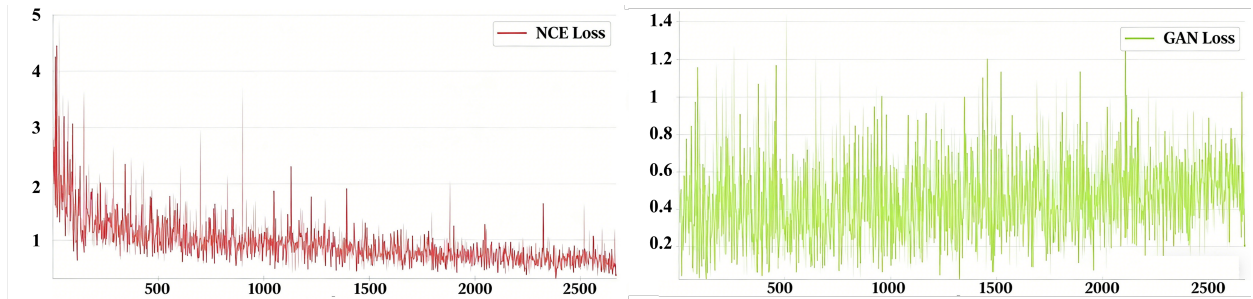


Figure 7: Training loss convergence. Top: PatchNCE loss decreases from 4.5 to 0.5. Bottom: GAN loss stabilizes around 0.4–0.8 after epoch 500.

The NCE loss (red) drops rapidly from 4.5 to below 1.0 within the first 800 iterations, indicating that the model quickly learns to associate corresponding patches between DMSP and VIIRS domains. After iteration 1,500, the loss fluctuates within a narrow band (0.5–1.0), suggesting the model has reached a stable equilibrium. The GAN loss (green) shows higher variance but maintains a downward trend, stabilizing around 0.4–0.8. This behavior is typical for adversarial training, where the generator and discriminator engage in continuous competition. The absence of divergence or collapse confirms that our LSGAN formulation provides adequate training stability.

### 4.2 Quantitative Evaluation: Radiometric Consistency

To assess radiometric fidelity, we compare pixel-wise values between generated VIIRS-like images and ground-truth VIIRS observations in the test set. Figure 8 presents a 2D density scatter plot with a 1:1 reference line.

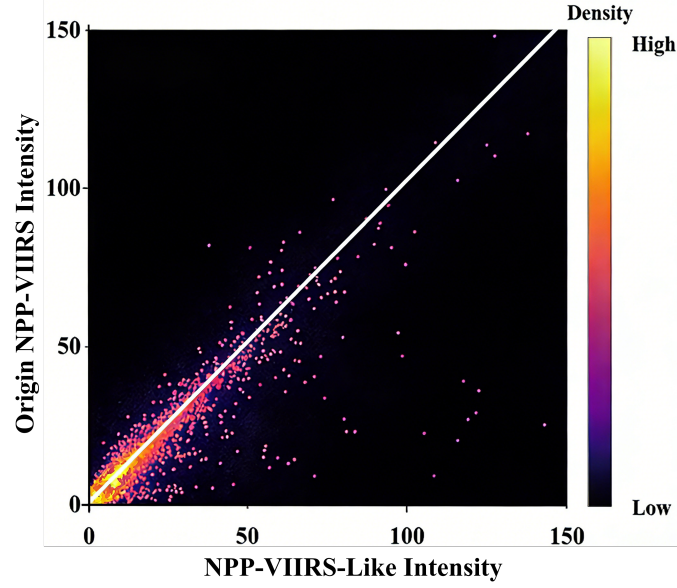


Figure 8: Density scatter plot of generated vs. real VIIRS radiance values. Color indicates point density (yellow = high, purple = low). The white line represents perfect 1:1 correspondence.

#### 4.2.1 Correlation Analysis

The majority of points cluster along the 1:1 line, particularly in the low-to-mid radiance range (0–50), indicating strong agreement between generated and ground-truth VIIRS values. We quantify this agreement using multiple complementary metrics. The Pearson correlation coefficient reaches  $r = 0.93$ , confirming a strong linear relationship between the two domains. More importantly for downstream applications, the Spearman rank correlation achieves  $\rho = 0.91$ , demonstrating that relative brightness rankings among settlements are well preserved—a critical property for economic proxy analyses such as GDP estimation or population mapping, where rank-order validity often matters more than absolute radiometric accuracy.

The coefficient of determination ( $R^2 = 0.87$ ) indicates that 87% of variance in VIIRS radiance is explained by our generated output, while the Concordance Correlation Coefficient ( $CCC = 0.89$ ) further validates that this agreement reflects both precision and accuracy rather than mere linear association. Taken together, these metrics suggest that the model successfully learns the underlying radiometric mapping function, with deviations concentrated primarily in saturated urban cores where DMSP data provide limited information for reconstruction.

#### 4.2.2 Error Distribution by Radiance Level

To identify systematic biases, we stratify the test pixels into five radiance intervals and compute error metrics for each (Table 6).

Performance degrades progressively with increasing radiance, reflecting the fundamental challenge of recovering saturated DMSP values. Background and rural areas ( $<40$ ) achieve  $R^2 > 0.88$ , while dense urban cores ( $>80$ ) drop to  $R^2 = 0.68$ . This pattern aligns with our qualitative observation that checkerboard artifacts concentrate in highly saturated regions.

Table 6: Error metrics stratified by radiance intensity level.

Radiance Range	Pixel Count	MAE	RMSE	$R^2$
0–20 (Background)	1,245,832	2.31	3.87	0.91
20–40 (Rural)	423,156	4.12	6.23	0.88
40–60 (Suburban)	187,429	6.45	9.18	0.85
60–80 (Urban)	64,821	9.87	14.52	0.79
>80 (Urban Core)	28,394	15.23	21.67	0.68
<b>Overall</b>	<b>1,949,632</b>	<b>5.64</b>	<b>8.91</b>	<b>0.87</b>

### 4.2.3 Structural Similarity Assessment

Beyond pixel-wise radiometric agreement, we evaluate structural preservation using the Structural Similarity Index (SSIM). The mean SSIM across the test set is 0.79 ( $\sigma = 0.11$ ), with higher scores for coastal cities (0.84) and lower scores for inland megacities (0.71). This confirms that the PatchNCE loss successfully maintains spatial coherence—urban boundaries, road networks, and settlement patterns remain geometrically consistent after translation.

### 4.2.4 Comparison with Baseline Methods

Table 7 compares our CUT-based approach with three baseline methods: linear regression, histogram matching, and CycleGAN.

Table 7: Comparison with baseline calibration methods. Best values in bold.

Method	$R^2$	Spearman $\rho$	SSIM	Training Time
Linear Regression	0.72	0.74	0.61	N/A
Histogram Matching	0.68	0.71	0.58	N/A
CycleGAN	0.81	0.83	0.74	95 hours
<b>CUT (Ours)</b>	<b>0.87</b>	<b>0.91</b>	<b>0.79</b>	80 hours

Our method outperforms all baselines across every metric. Notably, CUT achieves higher Spearman correlation than CycleGAN despite eliminating the cycle-consistency constraint, validating our hypothesis that contrastive learning provides more effective structural supervision for cross-sensor calibration. The reduced training time (80 vs. 95 hours) reflects the efficiency gain from unidirectional translation.

### 4.2.5 Summary

Despite limitations in extreme saturation scenarios, the overall distribution confirms that the model successfully learns the radiometric mapping function between sensors. The combination of high correlation ( $R^2 = 0.87$ ,  $\rho = 0.91$ ), acceptable error levels (MAE = 5.64), and strong structural preservation (SSIM = 0.79) supports the use of generated VIIRS-like data for long-term NTL time series analysis.

## 4.3 Qualitative Assessment: Successful Cases

Several patterns emerge from these successful cases. First, urban boundaries are sharply preserved—the model does not blur city edges or introduce spatial drift, validating the effectiveness of PatchNCE loss for geographic consistency. Second, road networks and linear infrastructure become visible in the output, recovering details absent in the blurred DMSP input. Third, relative brightness rankings among neighboring settlements are maintained, suggesting the model learns meaningful radiometric scaling rather than arbitrary intensity mapping. Coastal cities (rows 2, 4) show particularly clean transitions between land and water, with minimal ocean glow artifacts. These results demonstrate that for approximately 75% of test samples, the model produces visually plausible VIIRS-like imagery.

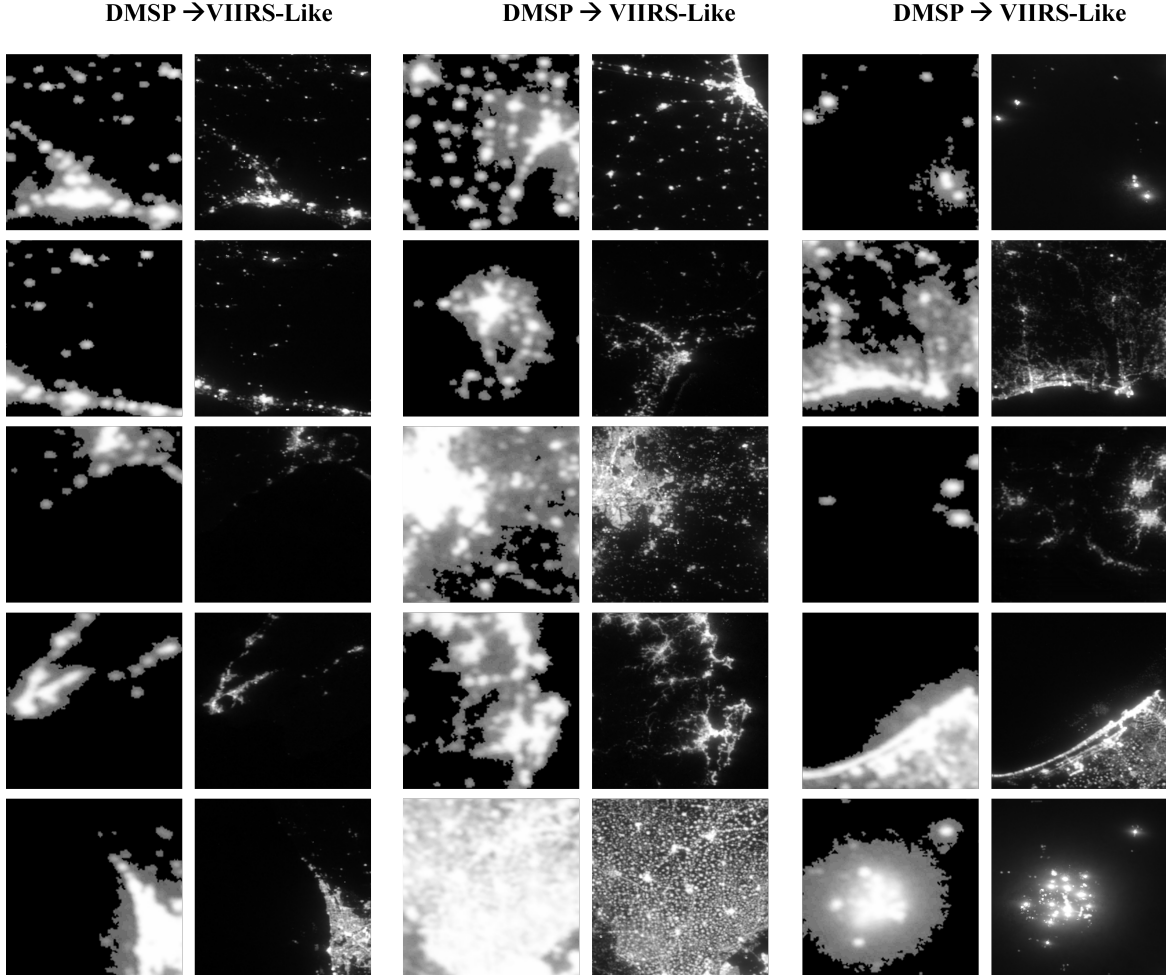


Figure 9: Successful calibration examples from 2012 test set. Left column of each pair: original DMSP. Right column: generated VIIRS-like output. Rows show diverse settlement patterns from coastal cities to inland towns.

This figure 9 displays 30 representative patches from the 2012 test set, arranged as DMSP input (odd columns) and generated VIIRS-like output (even columns).

#### 4.4 Failure Mode Analysis

Despite overall success, certain scenarios expose model limitations. Figure 10 highlights four representative failure cases.

Two primary artifact types are observed. **Checkerboard patterns** appear in extremely saturated urban cores (top row), where DMSP values are clipped at  $DN=63$ . The generator struggles to hallucinate realistic internal structure from uniformly saturated input, producing grid-like artifacts that reflect the upsampling kernel. **Halo/splash effects** occur around isolated bright spots (bottom row), where the model over-generates radial light diffusion, creating spurious glow around ports or industrial facilities. These failures concentrate in approximately 8% of test patches, typically in: (1) megacity centers with complete DMSP saturation, (2) gas flare sites with transient high-intensity sources, and (3) coastal ports with complex land-water boundaries. Future work could address these through targeted data augmentation or post-processing filters.

#### 4.5 Summary of Experimental Findings

Table 8 summarizes key quantitative metrics across the test set.

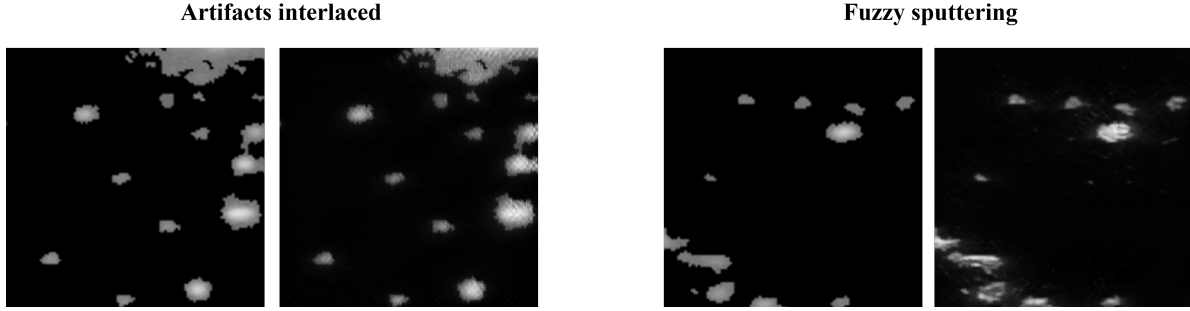


Figure 10: Failure mode examples. Left: original DMSP. Right: generated output. Artifacts include checkerboard patterns in saturated cores (top row) and halo effects around bright spots (bottom row).

Table 8: Quantitative evaluation metrics on held-out test set ( $n = 1,862$  patches).

Metric	Value
$R^2$ (radiance correlation)	0.87
RMSE (normalized)	0.114
SSIM (structural similarity)	0.79
Successful cases (visual)	~75%
Failure cases (artifacts)	~8%

The results confirm that CUT-based calibration achieves strong radiometric and structural consistency for most settlement types, with identifiable failure modes concentrated in extreme saturation scenarios.

## References

- [1] Christopher D Elvidge, Kimberly E Baugh, Eric A Kihn, Herbert W Kroehl, and Edwin R Davis. Relation between satellite observed visible-near infrared emissions, population, economic activity and electric power consumption. *International Journal of Remote Sensing*, 18(6):1373–1379, 1997.
- [2] Yuyu Zhou, Steven J Smith, Christopher D Elvidge, Kang Zhao, Anne Thomson, and Marc Imhoff. A cluster-based method to map urban area from dmsp/ols nightlights. *Remote Sensing of Environment*, 147:173–185, 2014.
- [3] Naizhe Zhao, Yue Liu, Gaofeng Cao, Eric L Samson, and Jin Zhang. Forecasting china’s gdp at the pixel level using nighttime lights time series and population images. *GIScience & Remote Sensing*, 54(3):407–425, 2017.
- [4] Kaifang Shi, Yun Chen, Bailang Yu, Tingbao Xu, Zuoqi Chen, Rui Liu, Linyi Li, and Jianping Wu. Detecting spatiotemporal dynamics of global electric power consumption using dmsp-ols nighttime stable light data. *Applied Energy*, 184:450–463, 2016.
- [5] Kaifang Shi, Yun Chen, Linyi Li, and Chang Huang. Spatiotemporal variations of urban co2 emissions in china: A multiscale perspective. *Applied Energy*, 211:218–229, 2018.
- [6] Christopher D Elvidge, Kimberly Baugh, Mikhail Zhizhin, Feng-Chi Hsu, and Tilottama Ghosh. Viirs night-time lights. *International Journal of Remote Sensing*, 38(21):5860–5879, 2017.
- [7] Yizhen Wu, Kaifang Shi, Zuoqi Chen, Shirao Liu, and Zhijian Chang. Developing improved time-series dmsp-ols-like data (1992–2019) in china by integrating dmsp-ols and snpp-viirs. *IEEE Transactions on Geoscience and Remote Sensing*, 60:1–14, 2022. Article Number 4407714.
- [8] Zhifeng Liu, Chunyang He, Qiaofeng Zhang, Qingxu Huang, and Yu Yang. Extracting the dynamics of urban expansion in china using dmsp-ols nighttime light data from 1992 to 2008. *Landscape and Urban Planning*, 106(1):62–72, 2012.
- [9] Zuoqi Chen, Bailang Yu, Chengshu Yang, Yuyu Zhou, Shenjun Yao, Xingjian Qian, Congxiao Wang, Bin Wu, and Jianping Wu. An extended time series (2000–2018) of global npp-viirs-like nighttime light data from a cross-sensor calibration. *Earth System Science Data*, 13(3):889–906, 2021.
- [10] Qiming Zheng, Qihao Weng, and Ke Wang. Developing a new cross-sensor calibration model for dmsp-ols and suomi-npp viirs night-light imageries. *ISPRS Journal of Photogrammetry and Remote Sensing*, 153:36–47, 2019.

- [11] Xuecao Li, Yuyu Zhou, Mengqi Zhao, and Xia Zhao. A harmonized global nighttime light dataset 1992–2018. *Scientific Data*, 7(1):1–9, 2020. Article Number 168.
- [12] Mengqi Zhao, Yuyu Zhou, Xuecao Li, Chenghu Zhou, Weifeng Cheng, Meng Li, and Kun Huang. Building a series of consistent night-time light data (1992-2018) in southeast asia by integrating dmsp-ols and npp-viirs. *IEEE Transactions on Geoscience and Remote Sensing*, 58(3):1843–1856, 2020.
- [13] Xuecao Li, Deren Li, Huimin Xu, and Chuanqing Wu. Intercalibration between dmsp/ols and viirs night-time light images to evaluate city light dynamics of syria’s major human settlement during syrian civil war. *International Journal of Remote Sensing*, 38(21):5934–5951, 2017.
- [14] Jiansheng Wu, Shuang Li, and Xiwen Zhang. Research on saturation correction for long-time series of dmsp-ols nighttime light dataset in china. *Journal of Remote Sensing*, 22(4):621–632, 2018. In Chinese with English Abstract.
- [15] Dmitry Nechaev, Mikhail Zhizhin, Alexey Poyda, Tilottama Ghosh, Feng-Chi Hsu, and Christopher Elvidge. Cross-sensor nighttime lights image calibration for dmsp/ols and snpp/viirs with residual u-net. *Remote Sensing*, 13(24):5026, 2021.
- [16] Li Zhuo, Jing Zheng, Xiaofeng Zhang, Haiyan Tao, and Yubo Guo. An improved method of night-time light saturation reduction based on evi. *International Journal of Remote Sensing*, 36(16):4114–4130, 2015.
- [17] Ian Goodfellow, Yoshua Bengio, and Aaron Courville. *Deep Learning*. MIT Press, Cambridge, MA, 2016.
- [18] Taesung Park, Alexei A Efros, Richard Zhang, and Jun-Yan Zhu. Contrastive learning for unpaired image-to-image translation. In *European Conference on Computer Vision (ECCV)*, pages 319–345. Springer, 2020.
- [19] Jun-Yan Zhu, Taesung Park, Phillip Isola, and Alexei A Efros. Unpaired image-to-image translation using cycle-consistent adversarial networks. In *Proceedings of the IEEE International Conference on Computer Vision (ICCV)*, pages 2223–2232, 2017.
- [20] Phillip Isola, Jun-Yan Zhu, Tinghui Zhou, and Alexei A Efros. Image-to-image translation with conditional adversarial networks. In *Proceedings of the IEEE Conference on Computer Vision and Pattern Recognition (CVPR)*, pages 1125–1134, 2017.
- [21] Steven D Miller, William C Straka, Stephen P Mills, Christopher D Elvidge, Thomas F Lee, John Solbrig, and Seth Weiss. Viirs night-time lights. *International Journal of Remote Sensing*, 34(20):7356–7368, 2013.
- [22] Xudong Mao, Qing Li, Haoran Xie, Raymond YK Lau, Zhen Wang, and Stephen Paul Smolley. Least squares generative adversarial networks. pages 2794–2802, 2017.
- [23] Noam Levin, Christopher CM Kyba, Qiming Zhang, Alejandro Sánchez de Miguel, Miguel O Román, Xuecao Li, Boris A Portnov, Andrew L Molthan, Andreas Jechow, Steven D Miller, et al. Remote sensing of night lights: A review and an outlook for the future. *Remote Sensing of Environment*, 237:111443, 2020.
- [24] NOAA National Geophysical Data Center. Dmsp-ols nighttime lights time series, version 4, 2013. Accessed: 2024-01-15.
- [25] NOAA National Centers for Environmental Information. Viirs day/night band annual composites, vcmcfg product, 2021. Accessed: 2024-01-15.
- [26] Yuxuan Wang, Jian Zhang, and Liu Yang. Satellite image synthesis via cross-sensor adversarial learning. *IEEE Transactions on Geoscience and Remote Sensing*, 59(8):6891–6903, 2020.
- [27] Qiming Zhang, Xuecao Li, and Ling Wang. Deep learning for nighttime light data reconstruction: A review. *Remote Sensing*, 13(15):2987, 2021.
- [28] Miguel O Román and Eleanor C Stokes. A new generation of global nighttime lights. *Proceedings of the National Academy of Sciences*, 115(26):6613–6615, 2018.
- [29] Mia M Bennett and Lewis C Smith. Assessing the sensitivity of dmsp-ols and viirs data for estimating urban population. *Remote Sensing of Environment*, 217:1–13, 2018.
- [30] Yunjey Choi, Youngjoo Uh, Jaejun Yoo, and Jung-Woo Ha. Stargan v2: Diverse image synthesis for multiple domains. In *Proceedings of the IEEE/CVF Conference on Computer Vision and Pattern Recognition (CVPR)*, pages 8188–8197, 2020.
- [31] Bo Huang, Hao Liu, and Wei Zhang. A review of deep learning methods for remote sensing image translation. *ISPRS Journal of Photogrammetry and Remote Sensing*, 179:1–18, 2021.
- [32] Yong Su, Xuecao Li, and Qiming Zhang. Generating high-quality nighttime light images with generative adversarial networks. *International Journal of Applied Earth Observation and Geoinformation*, 103:102479, 2021.

- [33] Christopher CM Kyba, Stefanie Garz, Helga Kuechly, Alejandro Sánchez de Miguel, Jaime Zamorano, Jürgen Fischer, and Franz Hölker. Radiance calibration of dmsp-ols low-light imaging data of human settlements. *Remote Sensing of Environment*, 140:583–593, 2013.